Elevation-Dependent Glacier Velocity and X-Band SAR Backscatter Indicate Seasonal and Topographic Controls on Tropical Glacier Dynamics in the Central and Southern Cordillera Blanca, Peru

Hannes Beier, Tazio Strozzi, *Senior Member, IEEE*, Julian Osten, Andrew Kos, *Member, IEEE*, and Florian Amann

***Abstract*—Tropical glacier dynamics are influenced by topography, near-surface thermodynamic conditions, basal processes indirectly reflected in surface motion, and climate variability, yet the regional-scale relationship between radar backscatter and glacier motion remains poorly constrained. We present a regional analysis of ice surface velocity and X-band synthetic aperture radar (SAR) backscatter across the central and southern Cordillera Blanca, Peru, using 72 high-resolution TerraSAR-X StripMap scenes acquired between December 2016 and May 2021. Ice surface velocities were derived from SAR intensity offset tracking, yielding a continuous 4.42-year record for 195 glaciers at an effective ground resolution of ∼60 m, with mean velocities ranging from 0.01 to 0.69 m d^{-1}. Radiometrically calibrated γ^0 backscatter shows strong seasonal and elevation-dependent variability, with pronounced annual amplitudes at mid-elevations (∼5000–5500 m a.s.l.) and nearly invariant signals above ∼5800 m a.s.l. While γ^0 decreases during the wet season, glacier velocities show recurrent dry-season accelerations. Correlations between detrended velocity residuals and precipitation are weak to moderate and spatially heterogeneous, whereas correlations with the Niño 3.4 index are spatially heterogeneous. In contrast, γ^0-precipitation correlations are predominantly negative, consistent with the sensitivity of X-band SAR to near-surface snow/firn moisture conditions. Cumulative displacement is predominantly linear over the 4.42-year observation period, with departures from linearity confined to dynamically complex sectors such as glacier tongues, crevassed basins, and areas adjacent to proglacial lakes. Overall, the results provide spatially distributed evidence for a vertically and seasonally stratified glacier response in the analyzed sectors: radar backscatter primarily reflects elevation- and season-dependent near-surface snow/firn conditions, whereas glacier surface velocity appears to be more strongly associated with glacier geometry and broader glacier-dynamic processes.**

***Index Terms*—Cordillera Blanca, ENSO, ice surface velocity, offset tracking, TerraSAR-X, tropical glaciers, X-band synthetic aperture radar (SAR) backscatter.**

I. Introduction

THE Cordillera Blanca is one of the major centers of tropical glaciation in the Andes and an important component of regional water resources for nearly four million people during the dry season [1]. Located in the outer tropical Andes (Fig. 1), its glaciers are close to the melting point and therefore respond rapidly to changes in temperature and precipitation. Tropical glaciers are characterized by strong climatic gradients and seasonally overlapping accumulation and ablation processes [2]. The regional climate is characterized by weak seasonal temperature variability, and a distinct wet (October–April) and dry (May–September) season governed by the Intertropical Convergence Zone [3]. Snow accumulation mainly occurs at higher elevations during the wet season, while ablation persists year-round, resulting in sustained glacier mass loss of approximately 0.4 m w.e. a^{-1} across the outer tropical Andes [3], [4], [5].

Beyond glacier retreat, ongoing mass loss modifies glacier geometry, thermal structure, and stress regimes, thereby influencing glacier dynamics. Variations in ice surface velocity are often linked to subglacial hydrology, as elevated basal water pressure reduces effective normal stress and enhances basal sliding, which may lead to transient accelerations in response to meltwater input or intense rainfall [6], [7], [8], [9], [10]. Seasonal and event-scale velocity fluctuations reflect the efficiency and temporal evolution of englacial and subglacial drainage systems [11], [12], [13], [14], [15], [16], [17]. At interannual timescales, large-scale climate variability such as the El Niño-Southern Oscillation has been suggested to influence glacier dynamics through changes in accumulation patterns and surface energy balance [18], [19]. However, the influence of ENSO on glacier dynamics remains complex and not fully understood. The relative contribution of basal sliding to surface motion varies

Received 26 February 2026; revised 17 May 2026 and 17 July 2026; accepted 28 July 2026. Date of publication 5 August 2026; date of current version 20 August 2026. This work was supported in part by through internal resources of the Chair of Engineering Geology and Hydrogeology, RWTH Aachen University and in part by the German Aerospace Center (DLR) provided TerraSAR-X data under proposal under Grant GEO3875. *(Corresponding author: Hannes Beier.)*

Hannes Beier and Julian Osten are with the Department of Engineering Geology and Hydrogeology, RWTH Aachen University, 52062 Aachen, Germany (e-mail: beier@lih.rwth-aachen.de; osten@lih.rwth-aachen.de).

Tazio Strozzi is with Gamma Remote Sensing Ltd., 3073 Gümligen, Switzerland (e-mail: strozzi@gamma-rs.ch).

Andrew Kos is with Terrasense Switzerland Ltd., 9470 Buchs, Switzerland (e-mail: andrew.kos@terrasense.ch).

Florian Amann is with the Department of Engineering Geology and Hydrogeology, RWTH Aachen University, 52062 Aachen, Germany, and also with the Fraunhofer Research Institution for Energy Infrastructures and Geotechnologies IEG, 52062 Aachen, Germany (e-mail: amann@lih.rwth-aachen.de).

This article has supplementary downloadable material available at https://doi.org/10.1109/JSTARS.2026.3719846, provided by the authors.

Digital Object Identifier 10.1109/JSTARS.2026.3719846

© 2026 The Authors. This work is licensed under a Creative Commons Attribution 4.0 License. For more information, see https://creativecommons.org/licenses/by/4.0/

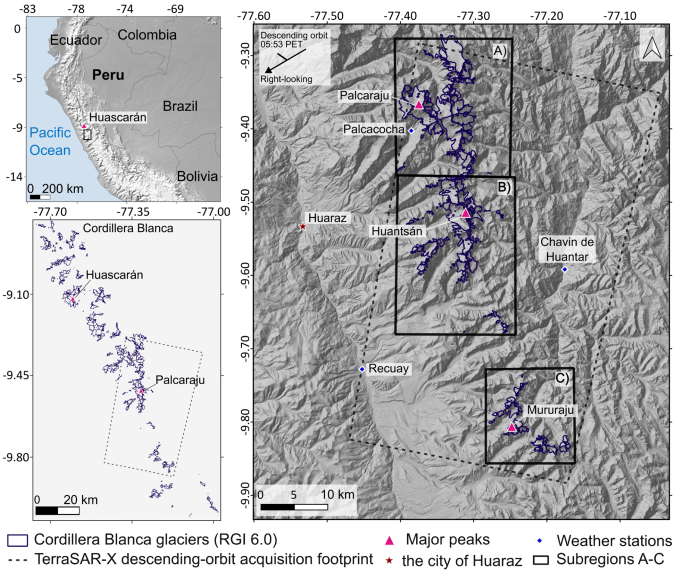


Fig. 1. Study area and TerraSAR-X coverage in the central and southern Cordillera Blanca, Peru. Insets show the location of the Cordillera Blanca within Peru and the distribution of RGI 6.0 glacier outlines along the range together with the approximate TerraSAR-X descending-orbit footprint. In the main panel, glacier outlines are shown in blue, the dashed polygon marks the analyzed TerraSAR-X footprint, and black rectangles delineate the three subregions used for regional analyses: (A) Palcaraju–Pucaranra, (B) Huantsán, and (C) Mururaju. The annotation indicates descending-orbit acquisition, right-looking geometry, and local acquisition time (∼05:53 PET). Major peaks, weather stations, and Huaraz are indicated for orientation. Background shading shows the AW3D30 digital surface model.

strongly with local geometry and bed conditions [20], [21]. Previous articles in the Cordillera Blanca and the tropical Andes have documented strong elevation-dependent glacier responses and climate sensitivity [1], [2], [22].

Changes in glacier dynamics have direct implications for hazards and water resources in the Cordillera Blanca. Unstable ice dams and heavily crevassed glacier tongues may fail catastrophically, triggering ice avalanches or glacial lake outburst floods, as illustrated by the 1941 Lake Palcacocha disaster in Huaraz [23], [24], [25]. In addition, dynamic changes influence seasonal runoff that supports irrigation, hydropower production, and downstream water supply. Despite extensive research on glacier mass balance and retreat in the tropical Andes, the regional-scale dynamic response of Cordillera Blanca glaciers remains incompletely understood, especially regarding the relationship between glacier motion, near-surface conditions, and climate variability. Few studies have jointly analyzed spatially distributed ice surface velocity and synthetic aperture radar (SAR) backscatter across multiple glaciers and elevation zones. Here, we jointly analyze TerraSAR-X-derived ice surface velocity and radiometrically calibrated X-band SAR backscatter (γ^0) across the central and southern sectors of the Cordillera Blanca. Spaceborne SAR enables spatially continuous observations of glacier motion and near-surface conditions independent of cloud cover and illumination, making it particularly suitable for tropical mountain environments.

We separate long-term ice surface motion from short-term variability and explore relationships between detrended

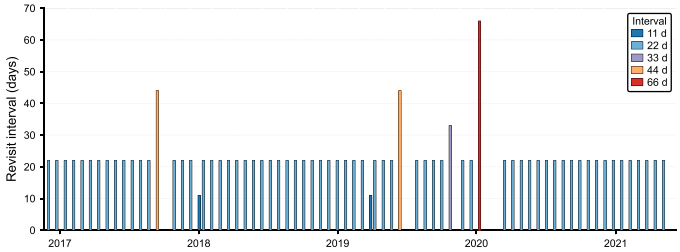


Fig. 2. Revisit intervals between consecutive TerraSAR-X acquisitions over the observation period from December 2016 to May 2021. Bars indicate the number of days between consecutive acquisitions and are color-coded by interval length. Most acquisitions follow the nominal 22-day repeat interval, while occasional shorter and longer intervals (11, 33, 44, and 66 days) reflect acquisition scheduling constraints and define the temporal sampling used for offset tracking.

velocity anomalies, precipitation, and potential ENSO-related co-variability (Niño 3.4 SST anomalies), while contrasting these patterns with γ^0–precipitation coupling. Specifically, we quantify: 1) spatial and topographic controls on mean glacier velocity, 2) seasonal differences between wet and dry seasons, 3) the linearity of glacier displacement and localized dynamic variability, and 4) the degree of coupling between surface conditions and glacier dynamics.

II. Materials and Methods

A. SAR Data

Multitemporal SAR data acquired by the TerraSAR-X satellite were used to derive glacier surface velocities and radiometrically calibrated radar backscatter across the analyzed central and southern sectors of the Cordillera Blanca. SAR data were used in two complementary ways: SAR intensity images were exploited to derive glacier surface velocities using offset tracking, while radiometrically calibrated backscatter (γ^0) was used to characterize elevation- and season-dependent surface conditions, including variations related to surface roughness and near-surface moisture conditions [26], [27], [28].

The dataset spans the period from 2 December 2016 to 29 May 2021 and consists of 72 TerraSAR-X StripMap scenes acquired in HH polarization, with a bandwidth of 150 MHz and a wavelength of 3.1 cm. All scenes were acquired at 10:52:55 UTC ($\pm$1 min; ∼05:53 Peru Time, PET) in descending orbit, corresponding to a NE–SW ground track and right-looking geometry, ensuring consistent acquisition geometry throughout the time series. Only one orbit direction was used to ensure consistent viewing geometry across the time series. This may have resulted in reduced data coverage in areas affected by layover and radar shadowing in steep terrain. TerraSAR-X StripMap pixel spacing is approximately 0.9 m in ground range and 2.0 m in azimuth, corresponding to a nominal spatial resolution of ∼3 m, which is well suited for resolving the small, steep, and spatially heterogeneous glaciers of the Cordillera Blanca. Revisit intervals follow TerraSAR-X repeat-cycle multiples for the selected orbit. Most acquisitions are separated by 22 days, with additional intervals of 11, 33, 44, and 66 days resulting from acquisition scheduling constraints. The resulting time series provides a continuous observational record of 4.42 years (Fig. 2). The dataset primarily

covers the central and southern Cordillera Blanca and does not include the full mountain range. In particular, parts of the northern Cordillera Blanca, including major glacierized areas around Huascarán, Huandoy, Artesonraju, Santa Cruz, and Safuna, are not covered due to acquisition constraints. Consequently, the results should be interpreted as representative of the analyzed central and southern sectors rather than the entire Cordillera Blanca.

For regional analysis, the study area was subdivided into three sectors (Fig. 1): Region A in the northern part of the analyzed TerraSAR-X footprint (Palcaraju area), Region B in the central range around Huantsán, and Region C in the southern Mururaju area. The use of a single descending orbit ensures consistent viewing geometry but may introduce aspect-dependent data gaps due to layover and radar shadowing in steep terrain. As a result, data coverage is not uniform across all glacier aspects. While ascending acquisitions could complement this limitation, they were not available consistently for the study period. The resulting dataset therefore represents a tradeoff between spatial coverage and temporal consistency, and the analysis focuses on regions with sufficient data availability.

B. DSM and Randolph Glacier Inventory

SAR geocoding, terrain correction, and topographic analyses were performed using the ALOS World three-dimensional (3-D) digital surface model (AW3D30), which provides a nominal spatial resolution of 30 m and was obtained from JAXA/EORC [29]. The digital surface model was used for SAR processing and to derive elevation bands and surface slopes required for analyses of topographic controls on ice surface velocity.

AW3D30 was selected due to its widespread use in glacier remote sensing, consistent performance in mountainous terrain, and compatibility with previous studies in the Cordillera Blanca [30]. Although higher resolution global digital elevation models such as TanDEM-X and the Copernicus DEM [31] exist, their restricted accessibility or recent release limit reproducibility and comparability with earlier work. A brief comparison between AW3D30 and the Copernicus DEM over the study area suggests no material differences at the spatial scales considered here (median elevation difference -4.6 m). These differences are small relative to the elevation bands used in the analysis and are therefore not expected to affect the main results.

Glacier extents were defined using outlines from the Randolph Glacier Inventory version 6.0 [32], which was the most recent release available when this study was initiated. Although these outlines predate the SAR observation period, differences relative to later RGI releases are mainly confined to glacier termini and margins, where local velocity patterns may therefore be affected by the chosen inventory. To assess whether this could influence the interpretation of the regional velocity patterns, we performed a descriptive first-order comparison between RGI version 6.0 [32] and RGI version 7.0 [33] for the valid TerraSAR-X displacement points. This comparison indicates that more than 95% of valid displacement points are consistently classified as glacierized in both inventories. AW3D30 was used as the DEM source for topographic extraction, whereas the RGI outlines were used solely to define glacier masks for sampling and did not affect SAR processing or the derivation of displacement fields. Taken together, the preceding DEM comparison and the RGI overlap analysis indicate that the choice of AW3D30 and RGI 6.0 is unlikely to materially affect the derived elevation-band statistics or the main regional ice-velocity patterns, while local tongue-scale differences should be interpreted with caution.

C. Meteorological Data

Daily meteorological observations were obtained from stations operated by the Servicio Nacional de Meteorología e Hidrología del Perú and the Instituto Nacional de Investigación en Glaciares y Ecosistemas de Montaña (INAIGEM). Daily precipitation totals and daily minimum and maximum air temperatures were extracted from the Recuay station ($\sim$3430 m a.s.l.) and the Chavín de Huantar station ($\sim$3170 m a.s.l.), representing lower elevation valley conditions surrounding the Cordillera Blanca. These records were complemented by high-elevation observations from the Palcacocha station ($\sim$4560 m a.s.l.), operated by INAIGEM.

Station selection was based on proximity to the study area and data availability. All meteorological records contain gaps due to instrument outages or quality-control filtering. While the Palcacocha station exhibits longer data gaps, it provides useful information on meteorological conditions closer to glacier accumulation zones that are not captured by valley stations and are therefore essential for interpreting glacier dynamics at higher elevations (Fig. 3). These station data represent lower- to mid-elevation conditions and may not fully capture meteorological variability at glacier elevations. They are therefore interpreted as indicative of regional meteorological variability rather than direct on-glacier conditions.

D. SAR Offset Tracking

Repeat-pass SAR has long been used to retrieve glacier motion and, in some cases, 3-D flow components from radar observations [34]. Here, glacier surface displacements were derived from TerraSAR-X intensity images using SAR offset tracking implemented in the GAMMA software package [35]. Offset tracking estimates surface displacement by cross-correlating stable backscatter patterns between consecutive SAR acquisitions. It remains robust under temporal decorrelation from surface melt, snowfall, or rapid glacier motion. TerraSAR-X data were processed into surface-displacement maps using the intensity offset-tracking method, also referred to as the cross-correlation optimization technique [27], [36]. In tropical mountain environments, temporal decorrelation frequently limits phase-based interferometric SAR (InSAR) measurements. We therefore used amplitude offset tracking, which remains robust under snowfall/melt and fast motion. A 2-D displacement approach was applied because consistently available multigeometry SAR acquisitions, which would be required for full 3-D decomposition, were not available for the study period.

Normalized cross-correlation was computed in slant-range geometry using moving windows of 128 $\times$ 96 pixels ($\sim$202 m $\times$ 192 m after ground-range projection) and a step size of 16

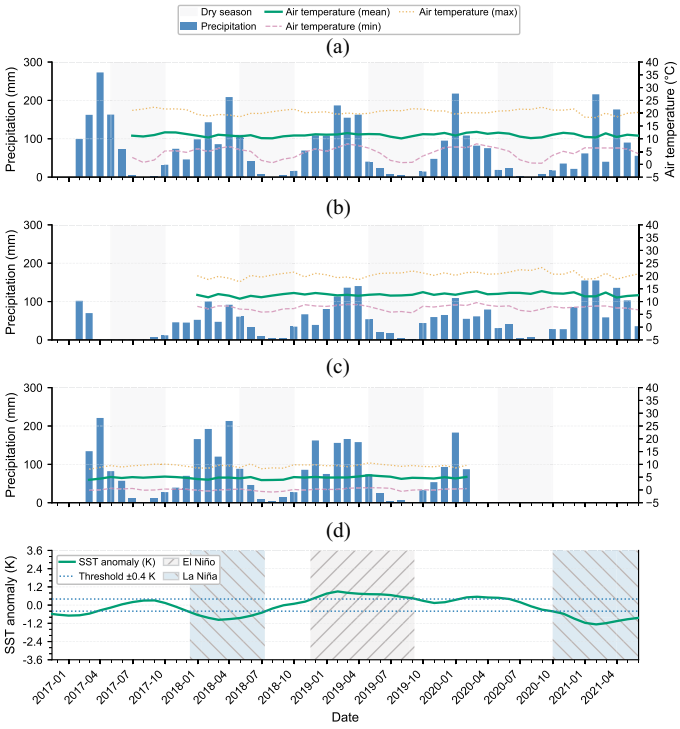


Fig. 3. Monthly precipitation and air temperature measured at three meteorological stations near the study area. (a) Recuay weather station (altitude: 3431 m a.s.l., coordinates: 09°43′45.1″ S, 77°27′13.15″ W). (b) Chavín de Huantar weather station (altitude: 3140 m a.s.l., coordinates: 09°35′9.54″ S, 77°10′30.94″ W), and (c) Palcacocha weather station (altitude: 4607 m a.s.l., coordinates: 09°24′09.3211″ S, 77°23′07.0258″ W), for the period 2017–2021. Bars indicate monthly precipitation totals, and lines indicate mean, minimum, and maximum air temperature. Shaded areas indicate the regional dry season (May–September). Data gaps, most pronounced at the high-elevation Palcacocha station, reflect instrument outages and quality-control filtering. (d) Sea surface temperature (SST) anomalies associated with the El Niño–Southern Oscillation (ENSO); El Niño and La Niña phases are highlighted based on a ±0.4 K threshold.

× 12 pixels (∼25 m × 24 m on the ground). The resulting displacement fields were geocoded using the AW3D30 digital surface model, yielding velocity maps with an effective ground resolution of ∼60 m. Subpixel offsets were obtained through biquadratic interpolation of the correlation peak. Displacements were converted to ice surface velocities by dividing by the temporal baseline of each acquisition pair and are reported in meters per day (m d^{-1}). Velocity uncertainty was estimated assuming an offset precision of ∼0.1 pixel, corresponding to ∼0.03–0.04 m d^{-1} for the shortest (11-day) repeat intervals [27], [30]. Iterative filtering based on correlation thresholds, angular deviation, and displacement magnitude was applied, and final velocity values were extracted for grid cells within RGI 6.0 glacier outlines. This 2-D surface displacement assumption is commonly applied in regional-scale glacier studies, but additional uncertainties may arise in steep terrain from geometric distortions and projection effects, particularly for small glaciers [27], [37], [38].

E. Backscatter SAR Data

Radiometrically calibrated TerraSAR-X X-band SAR backscatter (γ^0) was used to characterize temporal changes in near-surface snow and ice conditions. Radiometric calibration was performed using the GAMMA software package. Sigma nought (σ^0), the radiometrically calibrated radar backscatter coefficient, was first computed and subsequently corrected for local incidence angle and pixel illumination effects. The two quantities γ^0 and σ^0 are related by $\sigma^0 = \gamma^0 \cos\theta$, where θ is the local incidence angle [39]. A 5 × 5 multilooking factor was applied to reduce speckle noise. Due to the short X-band wavelength (∼3.1 cm), radar penetration into snow and firn is limited, and γ^0 primarily represents near-surface conditions [40], [41]. γ^0 values were extracted on the same ∼60 m grid used for ice surface velocity sampling. Pixels with more than 75% missing or invalid values were excluded. Remaining pixels were grouped into 100-m elevation bands, and median γ^0 values were computed for each acquisition to generate elevation-time matrices for seasonal and interannual analysis. These interpretations are based on established relationships between X-band backscatter and near-surface snow and ice properties [28], [39], [42], [43], [44] and should be understood as indicative rather than direct measurements of physical conditions.

F. Statistical Analysis

Linear regression models were fitted to cumulative glacier surface displacement time series for each grid cell over the full 4.42-year observation period following the residual-based approach of Kos et al. [30]. Regression slopes represent mean long-term displacement rates, and coefficients of determination (R^2) quantify goodness of fit. Residual time series were obtained by subtracting the fitted linear trend from the observed cumulative displacement. Only grid cells with at least 75% temporal coverage were retained; remaining gaps were filled using linear interpolation. This may introduce additional uncertainty in time series with larger data gaps. After filtering, 35 470 ice surface velocity time series and 35 849 γ^0 backscatter time series were available for analysis.

Pearson correlation coefficients were calculated between γ^0 backscatter and daily precipitation, and between velocity residuals and the Niño 3.4 sea-surface temperature index. These correlations are used to identify potential relationships and do not imply causality. All climate time series were temporally aligned to TerraSAR-X acquisition dates. Niño 3.4 sea-surface temperature anomalies were obtained from the NOAA Climate Prediction Center (CPC; Oceanic Niño Index / Niño 3.4), sampled at TerraSAR-X acquisition dates, and evaluated using a 3-month lag. This lag was used as an exploratory representation of delayed, seasonally integrated ENSO-related covariability, consistent with previously reported ENSO-related glacier responses in the tropical Andes [30]. The resulting correlations are used to describe spatial covariability and should not be interpreted as evidence of direct causality. Other lag times may also be relevant but were beyond the scope of this study. Given strong spatial autocorrelation, emphasis was placed on spatial patterns rather than grid-cell-level statistical significance.

Seasonal differences between wet and dry seasons were evaluated using a two-sided Mann–Whitney U test. To quantify topographic controls, velocity statistics were aggregated by 200-m elevation bands and 45° aspect sectors, including median

velocity and interquartile range (IQR). All analyses and visualizations were performed using Python and standard scientific computing libraries. Representative time-series locations were selected to illustrate recurring dynamic patterns rather than to define statistically independent glacier classes. The selected locations were grouped into descriptive dynamic settings using three criteria: 1) long-term mean velocity magnitude; 2) seasonal residual amplitude after removal of the linear displacement trend; and 3) geomorphological context visible in the velocity maps and topographic background (e.g., glacier tongues, crevassed glacier sectors, accumulation areas, and areas adjacent to proglacial lakes). These settings are therefore used for interpretation and visualization only and are not treated as formal glacier classes in the statistical analysis. Scientific color maps were used for visualization where appropriate [45].

III. Results

A. Spatial Patterns of Ice Surface Velocity

TerraSAR-X StripMap acquisitions between December 2016 and May 2021 comprise 72 scenes and 71 offset-tracking intervals, yielding a continuous observational record of 4.42 years and 71 displacement fields. Each interval contains on average ∼38 000 valid glacier grid cells. Mean ice surface velocities range from approximately 0.01 to 0.69 m d^{-1} (Fig. 4), consistent with previously reported values for glaciers in the analyzed parts of the Cordillera Blanca [30], [46].

The spatial distribution of long-term mean velocity exhibits pronounced regional contrasts (Fig. 4). Glaciers along the eastern side of the analyzed TerraSAR-X footprint generally show lower velocities, whereas higher velocities dominate the central and western parts of the analyzed sectors. The most dynamic glacier areas occur in subregion B, encompassing the steep and heavily glacierized terrain around Huantsán and adjacent glacierized areas. Elevated velocities are observed at mid-elevations between approximately 4900 and 5500 m a.s.l., where steep slopes coincide with well-developed flow corridors, although locally high velocities also occur at lower glacier elevations. Topographic patterns in glacier motion were quantified by aggregating velocity statistics by elevation band and slope aspect (Fig. 5). Median velocities and velocity variability, expressed as the IQR, are highest in low- to mid-elevation glacier zones, where steep slopes and well-developed flow corridors locally coincide with elevated velocities. At higher elevations, both metrics generally decrease or remain comparatively low.

A consistent aspect-related asymmetry is superimposed on the elevation dependence. North-, northwest-, and west-facing slopes exhibit higher median velocities and larger IQR values than south- and east-facing aspects across all elevation bands, with the strongest contrasts occurring at mid-elevations (Fig. 5). Velocity statistics as a function of surface slope indicate that the highest mean velocities occur on slopes between approximately 15° and 35°, whereas flatter terrain and very steep slopes are associated with lower average velocities (Fig. S1). The locally elevated median velocity around 5600 m a.s.l. in Fig. 5 is mainly expressed in specific aspect bins, particularly in west-

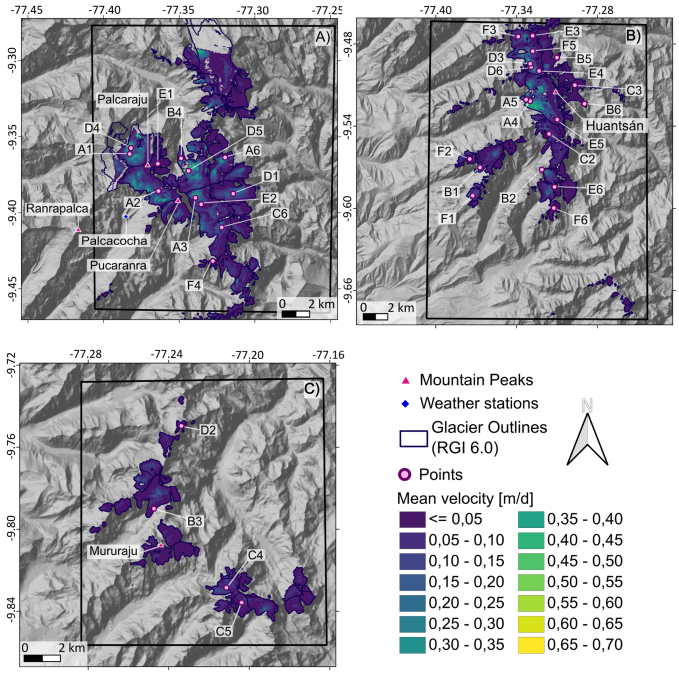


Fig. 4. Spatial distribution of long-term mean ice surface velocity derived from TerraSAR-X offset tracking for the period December 2016–May 2021. Panels show the three analyzed subregions: (A) Palcaraju–Pucaranra, (B) Huantsán, and (C) Mururaju. Colored glacier pixels represent mean surface velocity classes (m d^{-1}) averaged over the 4.42-year observation period. Glacier outlines are based on RGI 6.0. Magenta-outlined circles mark reference points selected for point-scale time-series analysis. Alphanumeric labels identify individual reference points and their descriptive dynamic setting: (A) highly crevassed shear margins; (B) lower ablation tongues; (C) snow-covered areas; (D) fast-flowing glacier zones; (E) slow-flow or stagnant glacier areas; and (F) western glacier sector. These labels are used consistently in Fig. 7, Fig. 10, and Table S1. Mountain peaks and weather stations are shown for orientation. The background shows hillshaded topography.

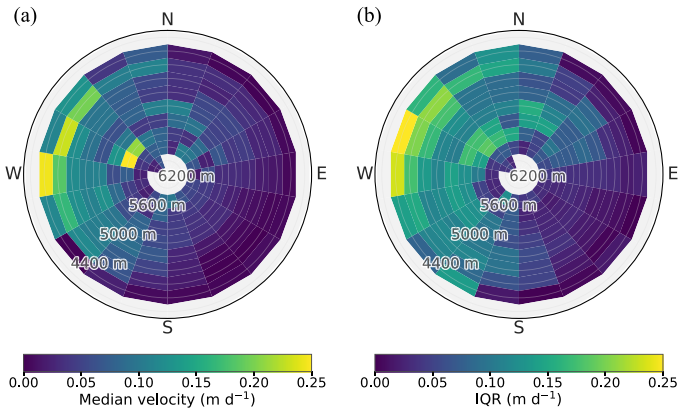


Fig. 5. Radial distributions of ice surface velocity statistics as a function of elevation and slope aspect across the analyzed central and southern sectors of the Cordillera Blanca. Polar plots show (a) median ice surface velocity (m d^{-1}) and (b) velocity variability expressed as the interquartile range (IQR, m d^{-1}), derived from TerraSAR-X offset-tracking observations over the full study period (2016–2021). Concentric rings represent 200 m elevation bands from ∼4400 to 6200 m a.s.l., with higher elevations toward the center, while angular sectors indicate glacier aspect (N, E, S, W). Colors denote the magnitude of each metric. The plots illustrate elevation- and aspect-dependent variability, with generally elevated velocities and variability at low to mid-elevations and systematically higher values on W–NW-facing slopes compared to E–S-facing aspects.

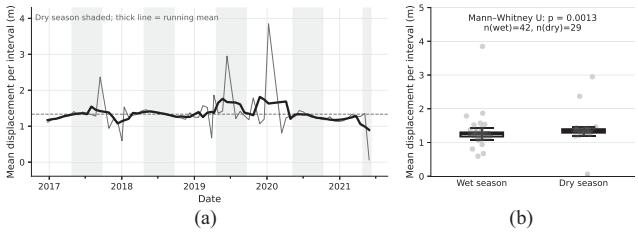


Fig. 6. Seasonal modulation of mean glacier displacement in the analyzed central and southern sectors of the Cordillera Blanca (TerraSAR-X, 2016–2021). (a) Regionally averaged mean glacier surface displacement per acquisition interval from late 2016 to May 2021. Thin grey lines show interval-to-interval mean displacements, the thick black line indicates a centered 5-interval running mean, and the dashed line denotes the long-term mean. Shaded areas mark the regional dry season (May–September). (b) Comparison of interval-mean displacement between the wet (October–April) and dry (May–September) seasons. Boxplots show the median and interquartile range; grey circles represent individual intervals. A two-sided Mann–Whitney U test indicates significantly higher displacement during the dry season ($p = 0.0013$; $n(\text{wet}) = 42$, $n(\text{dry}) = 29$).

to northwest-facing sectors, rather than across the full elevation band. This feature likely reflects local topographic and dynamic heterogeneity within the elevation-band aggregation and should therefore not be interpreted as a range-wide velocity maximum.

B. Seasonal Variability of Ice Surface Velocity

Regionally averaged mean glacier displacement per TerraSAR-X acquisition interval exhibits a recurring seasonal modulation (Fig. 6). Reference points shown in Fig. 4 correspond to the point-scale displacement time series presented in Fig. 7; the corresponding backscatter time series are presented later in the backscatter analysis. A total of 35 unique reference points were grouped into six descriptive dynamic settings (A–F) to illustrate the range of recurring velocity and backscatter behavior observed across the analyzed glacierized area. Letters denote the descriptive setting, whereas numbers identify individual reference points within each setting. The settings are: A, highly crevassed shear margins; B, lower ablation tongues; C, snow-covered areas; D, fast-flowing glacier zones; E, slow-flow or stagnant glacier areas; and F, western glacier sector. The corresponding labels, FIDs, and descriptive surface settings are listed in Table S1.

Mean displacement during the dry season (May–September) is approximately 7% higher than during the wet season (October–April). A two-sided Mann–Whitney U test confirms that dry- and wet-season displacement distributions differ significantly ($p = 0.0013$; Fig. 6). Time series extracted from selected grid-cell locations illustrate the spatial expression of this seasonal variability (Fig. 7, Fig. S9).

Selected locations represent descriptive dynamic settings defined by velocity magnitude, seasonal residual amplitude, and geomorphological context (Section II-F). They include steep accumulation zones, crevassed glacier sectors, glacier tongues, areas adjacent to proglacial lakes, and slow-flow or stagnant ablation areas (Fig. 7, Fig. S8). These locations were chosen to illustrate typical patterns observed across different glacier settings rather than to provide a complete classification; optical examples of the descriptive settings are provided in Fig. S13.

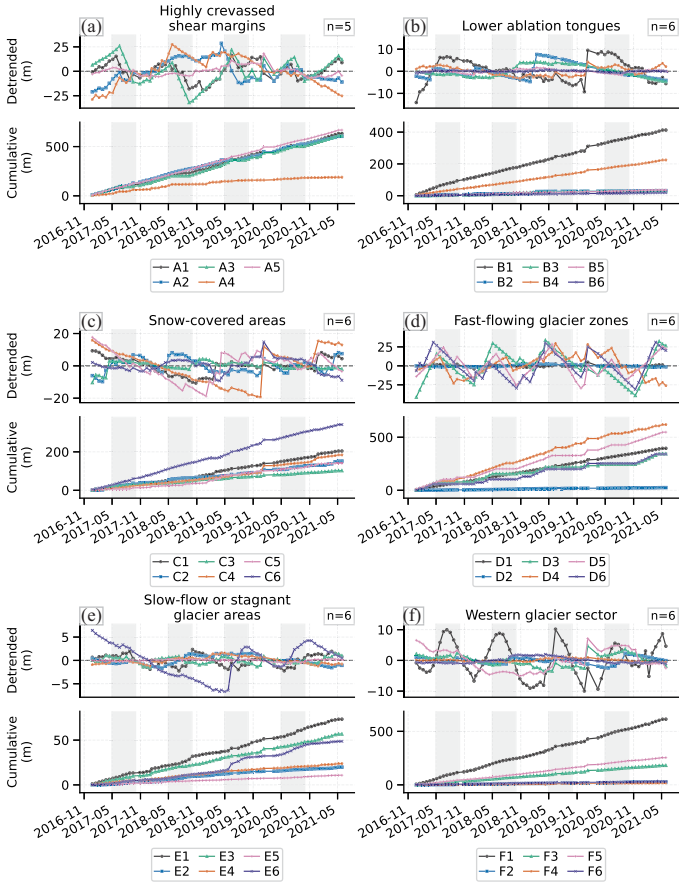


Fig. 7. Representative glacier surface displacement time series for selected reference points illustrating spatially heterogeneous seasonal variability across descriptive dynamic settings. For each panel, the upper subplot shows detrended displacement residuals, while the lower subplot shows cumulative surface displacement derived from TerraSAR-X offset tracking over the full observation period (December 2016–May 2021). Panels represent: (a) highly crevassed shear margins, (b) lower ablation tongues, (c) snow-covered areas, (d) fast-flowing glacier zones, (e) slow-flow or stagnant glacier areas, and (f) western glacier sector. Colored lines correspond to individual reference points labelled A1–F6; the corresponding FIDs and descriptive surface settings are listed in Table S1. Grey shading indicates the regional dry season (May–September). The examples illustrate recurring dry-season accelerations superimposed on largely linear long-term displacement trends, with substantial variability between glacier settings.

Fast-flowing and highly crevassed glacier sectors show recurring dry-season accelerations followed by stabilization or deceleration during the wet season. Seasonal displacement residual amplitudes at these locations typically range from 10 to 30 m per acquisition interval (11–66 days). In contrast, low-slope ablation tongues and dynamically stagnant glacier areas show subdued seasonal variability, generally below 5 m per interval. While dry-season acceleration represents the main regional pattern, localized deviations occur, particularly along the eastern side of the analyzed TerraSAR-X footprint, where some reference points exhibit reduced velocities during the dry season.

C. Linearity and Variability of Cumulative Displacement

Linear regression models fitted to cumulative displacement time series indicate that glacier motion across most of the analyzed glacierized area appears approximately linear over

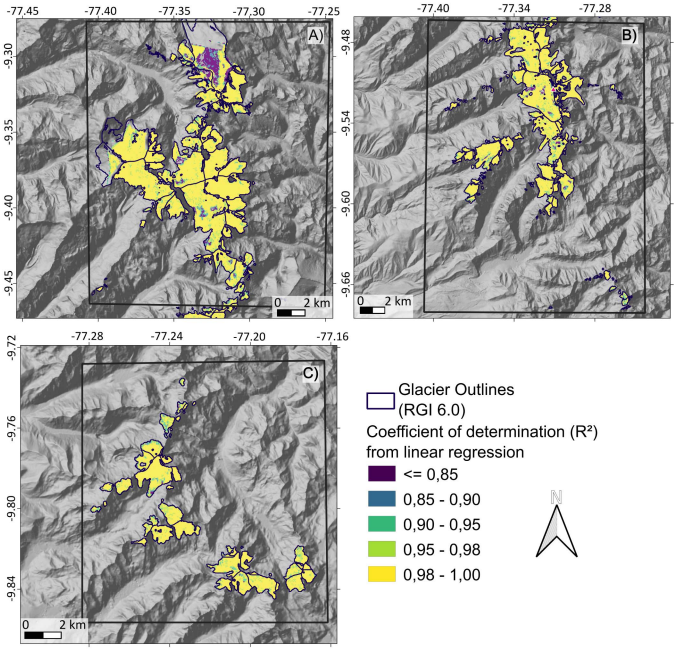


Fig. 8. Spatial distribution of the coefficient of determination (R^2) from linear regressions fitted to cumulative glacier surface displacement time series derived from TerraSAR-X offset tracking. R^2 values quantify the pixel-level goodness of fit of the linear displacement model over the 4.42-year observation period. Maps are shown for the three analyzed subregions: (A) Palcaraju–Pucaranra, (B) Huantsán, and (C) Mururaju. Colors indicate discrete R^2 bins. Glacier outlines are shown in blue and overlaid on a shaded digital elevation model. Scale bars and north arrows are provided for reference.

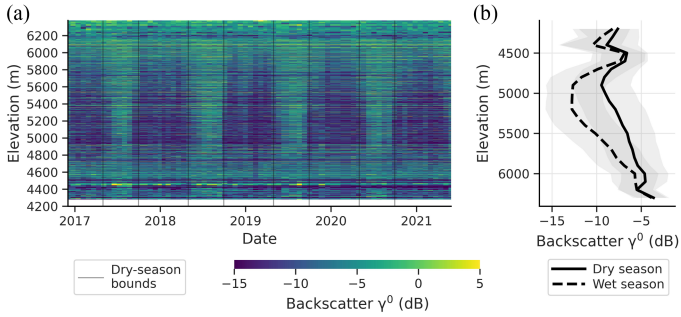


Fig. 9. TerraSAR-X X-band SAR backscatter (γ^0) variability over glacierized terrain in the analyzed central and southern sectors of the Cordillera Blanca. (a) Time–elevation diagram of radiometrically calibrated γ^0 backscatter from January 2017 to April 2021. Rows represent 100 m elevation bands and columns individual acquisition dates. Vertical grey lines mark the onset and end of the regional dry season (May–September). Seasonal γ^0 variability is strongest at mid-elevations (∼5000–5500 m a.s.l.) and weaker at high elevations above ∼5800 m a.s.l. (b) Seasonal elevation profiles of γ^0 derived from the same observations. Solid and dashed black lines show median γ^0 for the dry season (May–September) and wet season (October–April), respectively; grey envelopes indicate the interquartile range within 100-m elevation bands. The profiles show reduced wet-season γ^0 at low to mid elevations and limited seasonal contrast at higher elevations.

the 4.42-year observation period (Fig. 8). More than 80% of glacier grid cells exhibit coefficients of determination $R^2 \geq 0.95$, while approximately 11% show R^2 values below 0.89. Reduced R^2 values are spatially clustered along glacier tongues, near proglacial lakes, and within heavily crevassed accumulation basins. Grid cells affected by temporal data gaps also tend to exhibit lower R^2 values. Relative uncertainties, defined as the root mean square (rms) of regression residuals normalized by mean velocity, are highest where mean velocities are small. rms residuals indicate a limited subset of grid cells for which cumulative displacement deviates from a steady linear trend. These deviations are spatially coherent and primarily occur in dynamically active glacier sectors. Additional diagnostic relationships between velocity magnitude, regression quality, and uncertainty are provided in Fig. S2.

D. Spatiotemporal Variability of TerraSAR-X Backscatter

Radiometrically calibrated TerraSAR-X γ^0 backscatter exhibits pronounced seasonal and elevation-dependent variability across the analyzed central and southern sectors of the Cordillera Blanca (Fig. 9). Elevation-time analysis reveals systematic wet-season reductions of γ^0 at low to mid elevations between approximately 4300 and 5200 m a.s.l., with typical decreases of 6–10 dB that recur consistently from 2017 to 2021. During the dry season, γ^0 increases sharply, resulting in a robust annual cycle that is most pronounced between approximately 5000 and 5500 m a.s.l.

At elevations above approximately 5800 m a.s.l., γ^0 remains comparatively stable throughout the observation period, typically within a narrow range of -6 to -8 dB and with minimal seasonal or interannual variability. Seasonal γ^0 elevation profiles are consistent with this zonation (Figs. 9 and 10, Figs. S3 and S10). Wet-season γ^0 values are strongly reduced below about 5200 m, whereas dry-season γ^0 increases monotonically with elevation. Above approximately 5600 m, wet-season and dry-season profiles converge, indicating reduced seasonal variability at high elevations. Horizontal bands visible in the elevation-time backscatter diagrams reflect the distribution of glacier pixels within elevation bins rather than physical discontinuities. Temporal variability of γ^0, quantified as the standard deviation over time, decreases systematically with elevation (Fig. 9, Fig. S3) and falls below 2 dB above ∼5800 m a.s.l. Bedrock reference areas show negligible variability and no seasonal signal (Fig. S11).

E. Correlation Analyses of Detrended Velocity, Backscatter, and Meteorological Factors

To explore potential relationships between meteorological factors, particularly precipitation, and glacier dynamics, we performed correlation analyses between multiple variables. Specifically, we examined 1) the relationship between the residuals of the linear regression of ice surface velocities and precipitation data and 2) the relationship between γ^0 backscatter and precipitation.

In this article, absolute Pearson correlation coefficients $|r| < 0.3$ are interpreted as weak, $0.3 \leq |r| < 0.6$ as moderate, and $|r| \geq 0.6$ as strong relationships. All correlation maps represent spatial patterns of covariability derived from detrended time series and do not imply direct or predictive causal relationships. Correlation analyses were conducted between detrended ice surface velocity residuals and precipitation, between velocity

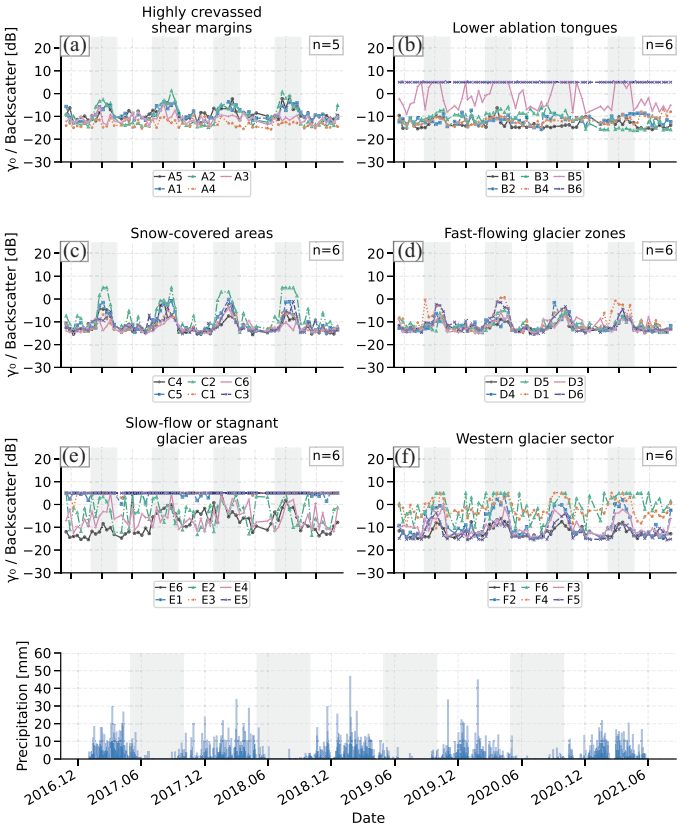


Fig. 10. Time series of TerraSAR-X radar backscatter (γ^0) at selected reference points illustrating spatially heterogeneous seasonal variability across different glacier settings. Panels correspond to the same descriptive settings and point labels as in Fig. 7 and Table S1: (a) highly crevassed shear margins, (b) lower ablation tongues, (c) snow-covered areas, (d) fast-flowing glacier zones, (e) slow-flow or stagnant glacier areas, and (f) western glacier sector. Colored lines represent individual reference points; the number of available points is indicated in each panel. Grey shading indicates the regional dry season (May–September). Daily precipitation is shown for climatic context only.

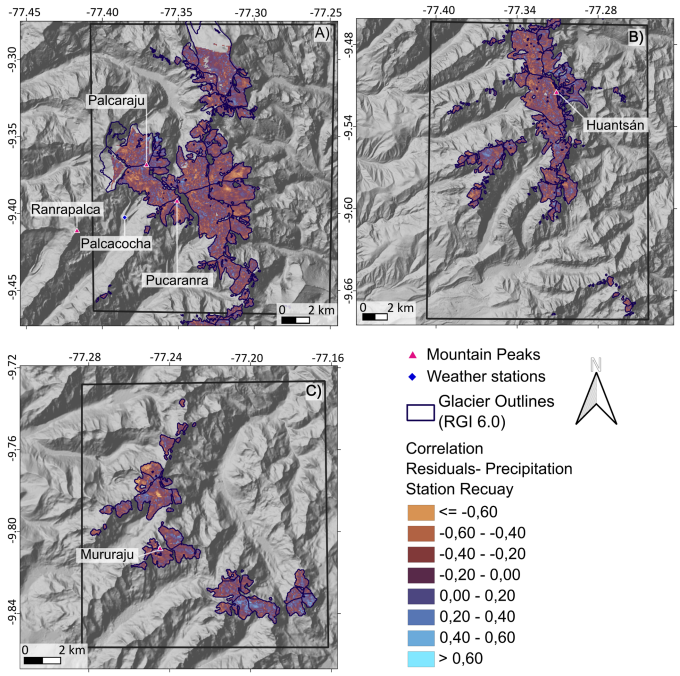


Fig. 11. Spatial distribution of Pearson correlation coefficients between detrended ice surface velocity residuals derived from TerraSAR-X offset tracking and daily precipitation measured at the Recuay meteorological station. Maps are shown for the three analyzed subregions: (A) Palcaraju–Pucaranra, (B) Huantsán, and (C) Mururaju. Colors indicate binned correlation coefficients. Glacier outlines from the Randolph Glacier Inventory (RGI 6.0) are shown in blue, mountain peaks are marked by triangles, and weather stations by diamonds. The background shows a shaded digital elevation model; scale bars and north arrows are provided for reference.

residuals and the ENSO Niño 3.4 index (3-month lag), and between γ^0 backscatter and precipitation.

Spatial correlations between velocity residuals and precipitation are weak to moderate and highly heterogeneous across the analyzed central and southern sectors of the Cordillera Blanca (Fig. 11). Correlation coefficients range from approximately −0.75 to +0.60 (Fig. S4), with most glacier pixels clustering near zero. Localized patches of positive and negative correlation occur primarily in dynamically active glacier sectors and show similar patterns across meteorological stations (Fig. S5).

Correlations between detrended velocity residuals and the Niño 3.4 index span a wide range (approximately −0.8 to +0.9; Fig. 12) and are spatially heterogeneous, with somewhat more spatial coherence than precipitation-based correlations (Fig. S4). Although predominantly weak to moderate, contiguous areas of stronger correlation occur locally, while the overall spatial pattern remains heterogeneous. The available correlation patterns do not provide clear evidence for a robust, systematic elevation dependence of the ENSO-related covariability; we therefore interpret the ENSO correlations primarily as spatially heterogeneous rather than as evidence of an elevation-controlled response.

In contrast, correlations between γ^0 backscatter and precipitation are predominantly negative and spatially coherent across all meteorological stations (Fig. 13, Fig. S6, and Fig. S7).

Together, Figs. 11–13 show that climate-related covariability differs between velocity and backscatter. Velocity residuals exhibit spatially heterogeneous and mostly weak-to-moderate correlations with precipitation and ENSO, whereas γ^0 backscatter shows a more coherent negative relationship with precipitation. This contrast supports the interpretation that X-band backscatter is primarily sensitive to near-surface snow/firn conditions, whereas glacier velocity reflects additional geometric controls and basal processes inferred indirectly from surface motion, which are not directly retrievable from X-band backscatter alone.

F. Coupled Variability of Surface Velocity and Backscatter

During the dry season, positive anomalies in both detrended ice surface velocity residuals and γ^0 backscatter are frequently observed, particularly within fast-flowing and highly crevassed glacier sectors (Fig. 14). γ^0 backscatter exhibits spatially coherent seasonal cycles across most glacierized areas, whereas velocity residuals vary more strongly between neighboring grid cells. The co-occurrence of positive γ^0 and velocity anomalies is observed most frequently in dynamically active zones and is less pronounced in slow-moving areas. Lag-correlation analyses

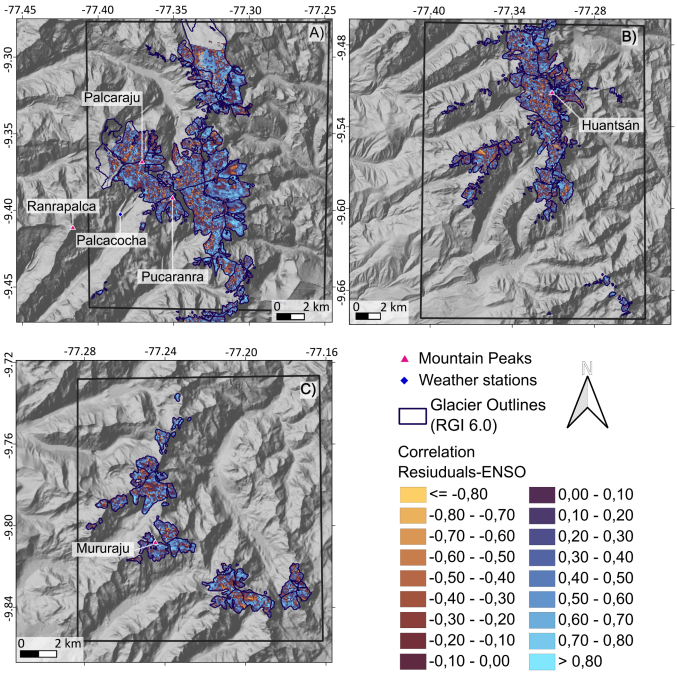


Fig. 12. Spatial distribution of Pearson correlation coefficients between detrended TerraSAR-X-derived ice surface velocity residuals and the Niño 3.4 index using a 3-month lag. Maps are shown for the three analyzed subregions: (A) Palcaraju–Pucaranra, (B) Huantsán, and (C) Mururaju. Colors indicate binned correlation coefficients, with warm colors representing negative correlations and cool colors representing positive correlations. Glacier outlines from the Randolph Glacier Inventory (RGI 6.0) are shown in blue; mountain peaks are marked by triangles and weather stations by diamonds. The background shows a shaded digital elevation model; scale bars and north arrows are provided for reference.

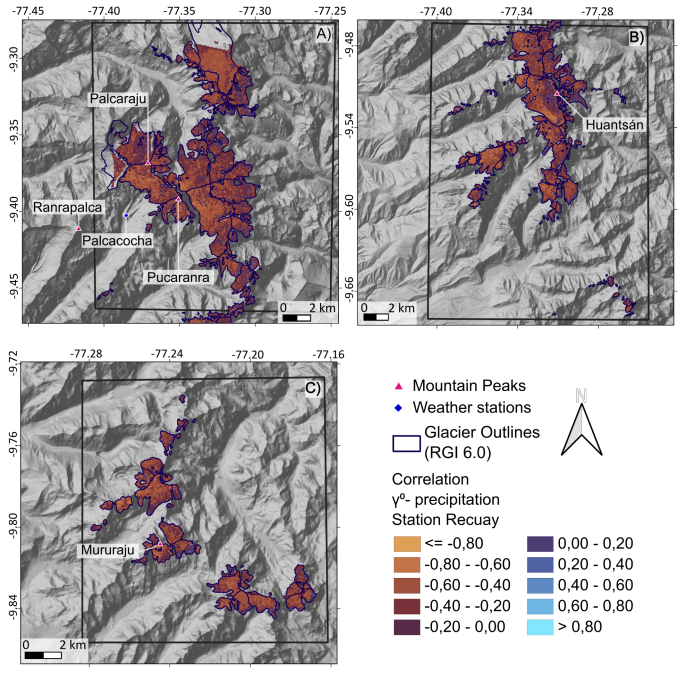


Fig. 13. Spatial distribution of Pearson correlation coefficients between TerraSAR-X γ^0 backscatter and daily precipitation measured at the Recuay meteorological station. Maps are shown for the three analyzed subregions: (A) Palcaraju–Pucaranra, (B) Huantsán, and (C) Mururaju. Colors indicate binned correlation coefficients, with negative values dominating across most glacierized areas. Glacier outlines from the Randolph Glacier Inventory (RGI 6.0) are shown in blue; mountain peaks are marked by triangles and weather stations by diamonds. The background shows a shaded digital elevation model; scale bars and north arrows are provided for reference.

indicate generally weak coupling for most grid cells ($|r| < 0.3$ for 85% of grid cells; Fig. S12).

IV. Discussion

Our multiyear (2016–2021) TerraSAR-X analysis of ice surface velocity and X-band SAR backscatter across the central and southern sectors of the Cordillera Blanca provides regional-scale insights into how glacier velocity and X-band backscatter vary with topography, near-surface conditions, and large-scale climate variability across the analyzed sectors. By combining spatial velocity patterns, seasonal variability, linearity diagnostics, and correlation analyses, our results suggest that radar backscatter and glacier motion respond differently to seasonal and elevation-dependent variability, with weak and spatially heterogeneous coupling at the point scale.

A. Climatic and Altitudinal Controls on Glacier Facies and Surface Conditions

At elevations above approximately 5800 m a.s.l., TerraSAR-X γ^0 backscatter remains nearly constant (typically -6 to -8 dB; Fig. 9), suggesting relatively dry and frozen firn conditions with limited seasonal melt. This behavior is consistent with high-elevation dry-snow and firn facies described in previous articles [43], [47]. The muted seasonality of both γ^0 and ice

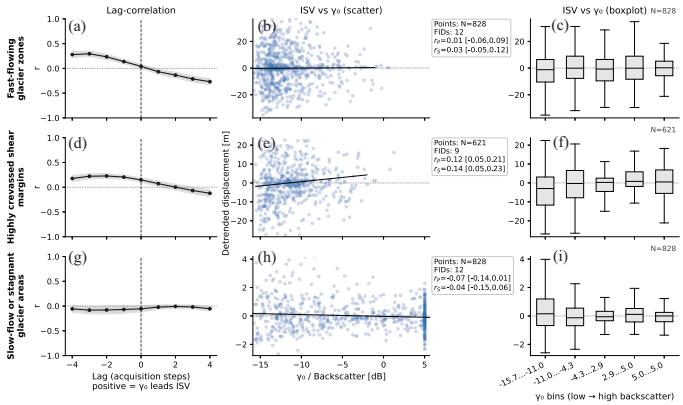


Fig. 14. Relationship between detrended ice surface velocity (ISV) and TerraSAR-X radar backscatter (γ^0) for three descriptive dynamic settings. Panels (a)–(c) show results for fast-flowing glacier zones, (d)–(f) for highly crevassed shear margins, and (g)–(i) for slow-flow or stagnant glacier areas. Panels (a), (d), (g) show lagged cross-correlations between γ^0 and ISV, where positive lag values indicate that γ^0 leads ISV; shaded envelopes denote the uncertainty range of the correlation coefficient. Panels (b), (e), (h) show scatter plots of detrended ISV versus γ^0 with linear regression fits; Pearson (r_p) and Spearman (r_s) correlation coefficients with 95% confidence intervals are reported. Panels (c, (f), (i) show boxplots of detrended ISV grouped into successive γ^0 bins from low to high backscatter. N denotes the number of paired observations, and FIDs denote the number of contributing reference-point locations.

surface velocity at these elevations is compatible with relatively dry or frozen firn conditions and limited seasonal hydrological forcing, although englacial and basal thermal conditions cannot be directly inferred from the present observations.

Despite this overall stability, locally moderate-to-strong correlations between velocity residuals and the ENSO Niño 3.4 index suggest that interannual climate variability may be associated with secondary velocity variability in some sectors. Such correlations may indicate an indirect and spatially heterogeneous ENSO-related influence on glacier dynamics, potentially mediated by accumulation and surface-energy-balance variability rather than by direct short-term meltwater forcing. The underlying mechanisms remain uncertain and cannot be resolved from the present dataset alone, consistent with previous articles of tropical Andean glaciers [1], [18], [19], [30]. For the Cordillera Blanca specifically, interannual glacier mass-balance variability has been linked to tropical Pacific variability and wet-season precipitation anomalies [1]. Recent observations from the tropical Andes further show that El Niño conditions can enhance snowline rise and ice loss, reinforcing the sensitivity of tropical glaciers to large-scale Pacific variability [48].

Between approximately 5000 and 5500 m a.s.l., both γ^0 backscatter and glacier velocity exhibit their strongest seasonal variability (Fig. 9). This elevation band coincides with the regional precipitation maximum [49], and broadly represents the transition between accumulation and ablation regimes. Seasonal γ^0 amplitudes of up to $\sim$10–15 dB reflect wet-season attenuation and dry-season enhancement associated with melt-refreeze cycles, changes in snow wetness, and evolving surface roughness and microstructure [50], [51], [52]. Surface melt and wet snow conditions are known to produce pronounced reductions in SAR backscatter signals in glacierized mountain regions [53].

Predominantly negative γ^0-precipitation correlations further support moisture-driven attenuation of X-band backscatter [28]. In contrast, velocity-precipitation correlations remain weak to moderate and spatially heterogeneous, implying that short-term precipitation variability alone explains only a limited fraction of regional velocity anomalies. This behavior may reflect redistribution and temporary storage of water within englacial and subglacial drainage systems prior to influencing basal motion [9], [54]. The spatial distribution of velocity-precipitation correlations is consistent with spatially variable hydrological sensitivity of glacier motion across different dynamic settings. In the mapped patterns, many faster moving glacier sectors show relatively weak or spatially less coherent correlations with precipitation. One possible explanation is that these sectors may contain more established or better connected englacial/subglacial drainage pathways, allowing additional water input to be accommodated without producing large or sustained increases in basal water pressure [12], [14], [16], [17], [55]. In contrast, some slower moving sectors, particularly in the Mururaju region, locally show stronger precipitation-related covariability. This pattern could be consistent with less efficient or more poorly connected drainage configurations, where water input can more readily increase basal water pressure, reduce effective pressure, and enhance basal sliding [9], [15], [17], [54]. Because basal conditions are not directly observed, this interpretation remains indirect, but it provides a physically consistent explanation for the observed spatial heterogeneity in the velocity–precipitation relationships.

The lagged Niño 3.4 analysis should therefore not be interpreted as a direct test of whether individual precipitation events immediately increase basal water pressure and enhance sliding. Rather, it should be viewed as an exploratory measure of delayed, seasonally integrated hydroclimatic covariability, potentially involving delayed storage, accumulation and firn processes, seasonal drainage evolution, and broader hydrological memory. The locally coherent Niño 3.4 correlation pattern east of Pucaranra may be consistent with spatially variable moisture delivery, although this interpretation remains tentative. In this sector, generally lower surface velocities coincide with locally stronger climate-related covariability, suggesting that slower moving glacier areas may preserve a clearer hydroclimatic signal than dynamically active sectors where geometry and internal glacier dynamics exert stronger control.

In the ablation zone below approximately 4500 m a.s.l., elevated γ^0 values ($>$0 dB) are consistent with exposed ice, roughened surfaces, and episodic supraglacial water accumulation [43], [55]. Observed seasonal velocity variations may be related to transient changes in basal water pressure within inefficient drainage systems rather than sustained increases in meltwater production, although this interpretation remains indirect and cannot be confirmed without direct observations [9], [21], [56]. Accordingly, co-occurrence of elevated γ^0 and enhanced velocities during the dry season does not imply a direct causal link.

Isolated high velocity values approaching 0.69 m d^{-1} should be interpreted in the context of regression diagnostics, which show that such extremes are spatially confined and do not represent basin-wide sustained acceleration. Overall, γ^0 provides a useful indicator of elevation-dependent near-surface state, whereas glacier velocity reflects geometric controls and basal processes inferred indirectly from surface motion, which are not directly retrievable from X-band backscatter alone. The early-morning acquisition time reduces the likelihood that the observed velocity variability reflects contemporaneous daytime surface melt at the acquisition time, but it does not by itself distinguish englacial from subglacial mechanisms.

B. Topographic and Aspect-Driven Variability

Topography is strongly associated with glacier velocity patterns across the analyzed central and southern sectors of the Cordillera Blanca by influencing surface slope, driving stress, and potential hydrological pathways [30]. Flatter glacier sections tend to respond more weakly due to lower hydraulic gradients and greater storage capacity, which buffer short-term variability [5], [57]. In contrast, very steep slopes, particularly in hanging glacier terrain, may be dominated by internal deformation and icefall processes, limiting the sensitivity of basal sliding to hydrological forcing [30]. Aspect-related contrasts likely reflect differences in radiation exposure and atmospheric forcing that indirectly influence glacier hydrology and rheology. This pattern is broadly consistent with aspect-controlled differences in radiation, shading, and cloud cover in the tropical Andes

[3], [58], which modulate surface energy balance and indirectly influence hydrological and rheological conditions. Topographic longwave radiation from adjacent terrain can locally enhance melt at glacier margins, contributing to spatially concentrated variability near glacier tongues and lateral margins [59].

C. Linearity, Stability, and Spatially Confined Dynamic Variability

The predominance of highly linear cumulative displacement time series over 4.42 years suggests that glacier motion across most of the analyzed glacierized area can be approximated by steady long-term velocities, consistent with previous articles of individual glaciers in the region [30].

However, the 4.42-year observation period may be insufficient to resolve longer term nonlinear trends associated with sustained glacier thinning. Regional geodetic studies indicate continued glacier thinning and mass loss across the tropical Andes and Peru, suggesting that approximately linear displacement over short observation periods does not preclude longer term dynamic or geometric changes [60], [61].

Spatial clustering of lower R^2 values along glacier tongues, near proglacial lakes, and within heavily crevassed accumulation basins indicates that nonsteady flow behavior appears to be concentrated in dynamically complex zones. Elevated relative uncertainties and rms residuals in these areas further suggest that departures from linearity are spatially coherent rather than random noise. While the 4.42-year observation period is sufficient to resolve persistent seasonal and interannual variability, longer time series would be required to robustly detect potential nonlinear trends associated with long-term geometric adjustment. As a result, residual variability likely reflects temporally integrated glacier responses.

D. Coupled Variability of Surface Velocity and Backscatter

The weak coupling between γ^0 backscatter and ice surface velocity suggests that γ^0 backscatter and ice surface velocity may respond differently to seasonal variability. X-band γ^0 mainly reflects near-surface thermodynamic and microstructural conditions, whereas ISV reflects geometric controls and basal processes inferred indirectly from surface motion. This interpretation is consistent with SAR-based studies showing that backscatter variability is sensitive to near-surface melt and moisture conditions [53]. Weak positive correlations in fast-flowing and crevassed sectors suggest that dry-season surface states may coincide with enhanced motion, but this covariability is indirect and spatially confined. Overall, the joint analysis shows that γ^0 and ISV respond differently to seasonal variability, with γ^0 primarily reflecting near-surface snow/firn conditions and ISV reflecting geometric controls and basal processes inferred indirectly from surface motion. Their point-scale coupling remains weak and spatially inconsistent, but together they provide complementary constraints on glacier surface state and spatial patterns of dynamic sensitivity.

Fig. 15 summarizes the inferred relationships between topography, seasonality, X-band backscatter, glacier surface velocity, and climate-related covariability, and provides a conceptual

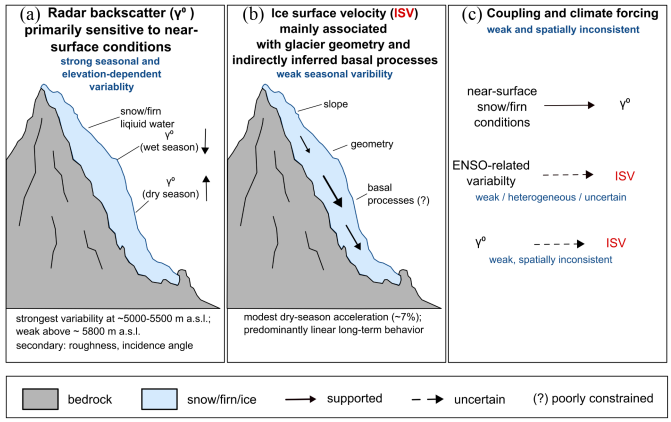


Fig. 15. Conceptual synthesis of controls on TerraSAR-X radar backscatter (γ^0) and ice surface velocity (ISV) in the central and southern Cordillera Blanca. (a) X-band γ^0 primarily reflects near-surface snow/firn conditions, with wet-season attenuation and dry-season enhancement strongest at mid-elevations. (b) ISV is mainly associated with glacier geometry, surface slope, and basal processes inferred indirectly from surface motion; seasonal velocity variability is comparatively weak, with a modest regional dry-season acceleration. (c) γ^0 and ISV show weak and spatially inconsistent coupling. ENSO-related variability is shown only as a weak, heterogeneous, and uncertain influence on ISV; no direct ENSO control on near-surface γ^0 conditions is implied. Solid arrows indicate supported relationships, dashed arrows indicate uncertain or heterogeneous links, and question marks denote poorly constrained processes.

synthesis of the main patterns identified in this article. At high elevations ($>\sim$5800 m a.s.l.), persistently low and weakly variable γ^0 values are consistent with predominantly dry and frozen firn conditions, suggestive of limited seasonal meltwater production and subdued velocity variability. At mid-elevations ($\sim$5000–5500 m a.s.l.), where γ^0 variability is strongest and accumulation–ablation transition conditions are likely to occur, γ^0 exhibits its strongest seasonal modulation, which may be related to changes in snow and firn liquid water content, while ice surface velocity shows spatially heterogeneous variability that may be partly related to seasonal and interannual climatic conditions. In contrast, at lower elevations ($<\sim$4500 m a.s.l.), elevated γ^0 values are commonly associated with exposed, rough ice surfaces and episodic supraglacial water storage, whereas velocity variability may be consistent with transient changes in basal water pressure or drainage efficiency, but this interpretation remains indirect because basal conditions were not observed. Aspect-related differences further modulate these patterns through asymmetric radiative forcing and atmospheric moisture input. Taken together, the schematic summarizes that seasonal γ^0 variability and ice surface velocity may partly respond to related seasonal variability, but their coupling remains weak and strongly dependent on elevation and local glacier geometry.

E. Regional and Global Context

Velocity magnitudes and spatial patterns observed in this article are consistent with previous investigations in the Cordillera Blanca and the tropical Andes [30], [46]. The pronounced spatial contrasts in glacier dynamics across the analyzed sectors are consistent with previous studies indicating that glacier geometry, aspect, topographic setting, and spatially variable hydroclimatic

conditions can modulate surface motion and dynamic activity in mountain glaciers [27], [30], [38], [42], [46], [62], [63]. However, these spatial contrasts should not be interpreted as evidence for a simple west–east precipitation gradient. Moisture supply to Peruvian glaciers is strongly influenced by easterly Amazonian moisture transport, while precipitation phase, cloud cover, and radiative forcing further modulate melt processes [64].

Seasonal to interannual velocity anomalies are broadly consistent with previously reported ENSO-related glacier responses documented in tropical regions, where El Niño and La Niña phases modulate accumulation and surface energy balance and thereby influence glacier flow indirectly [18], [19], [65]. These patterns are broadly consistent with observations from other tropical glacier regions, suggesting that elevation-dependent climate variability and hydrological processes may contribute to glacier dynamic variability across different mountain environments [18], [19], [65]. Comparable facies-sensitive SAR backscatter behavior has been reported for other mountain ranges [43], [51], and similar climate-related velocity variability has been observed in the Pamirs [66] and polar ice masses [67].

Geodetic observations show sustained glacier mass loss across Peru, with increased wastage after 2013 also affecting the Cordillera Blanca [4], [61]. Despite this continued mass loss, the predominance of approximately linear long-term displacement in our record suggests that progressive thinning has not yet produced a clear basin-wide dynamic slowdown over the 2016–2021 observation period. This apparent stability nevertheless coexists with spatially confined zones of enhanced variability, such as glacier tongues, crevassed basins, and areas adjacent to proglacial lakes, which may disproportionately contribute to transient dynamics and glacier-related hazards. Overall, the observed velocity patterns are broadly consistent with established glacier-dynamic concepts linking surface motion to glacier geometry and basal processes inferred indirectly from surface motion.

F. Methodological Considerations and Implications

Several limitations should be considered when interpreting the results. Projection of slant-range and azimuth offsets onto glacier-flow direction introduces uncertainty in steep and complex terrain, particularly for small or highly inclined glaciers. The limited penetration depth of X-band SAR constrains interpretation to near-surface processes, and the ∼22-day revisit interval limits detection of short-lived dynamic events [50], [68]. Because no direct field validation of snow wetness or surface moisture was available, γ^0 is interpreted as an indicator of near-surface conditions rather than a direct moisture measurement. Similarly, basal processes are inferred only indirectly from spatial and temporal velocity patterns and cannot be independently validated with the present dataset. Nevertheless, the agreement among spatial patterns, seasonal cycles, and regression diagnostics supports the main findings. Future work integrating multifrequency SAR observations with in situ measurements would improve separation of surface- and basal-driven processes and support more detailed interpretation of glacier hydrology.

Overall, the elevation- and climate-dependent patterns documented here are consistent with a combination of topographic effects, near-surface thermodynamics, basal processes inferred indirectly from surface motion, and large-scale climate variability across the analyzed sectors.

V. Conclusion

This article provides a regional-scale assessment of glacier surface dynamics and X-band SAR backscatter in the central and southern Cordillera Blanca using 72 TerraSAR-X StripMap acquisitions (2016–2021), yielding a continuous 4.42-year record for 195 glaciers. Cumulative displacement time series are predominantly linear, with departures from linearity primarily occurring in dynamically complex sectors (e.g., glacier tongues, crevassed basins, and areas near proglacial lakes).

Backscatter mainly reflects elevation- and season-dependent near-surface snow/firn conditions, whereas velocity anomalies show weaker and spatially heterogeneous relationships with meteorological and large-scale climate variability. This indicates that surface backscatter variability and glacier dynamics are only weakly coupled at the point scale. The presented time series provide a baseline for regional monitoring of glacier dynamics in the central and southern Cordillera Blanca. Continued SAR-based monitoring combined with updated elevation data and targeted field measurements can support improved assessments of glacier evolution, water availability, and glacier-related risks in the tropical Andes.

References

[1] M. Vuille et al., "Climate change and tropical Andean glaciers: Past, present and future," *Earth-Sci. Rev.*, vol. 89, no. 3–4, pp. 79–96, Aug. 2008, doi: 10.1016/j.earscirev.2008.04.002.

[2] G. Kaser and H. Osmaston, *Tropical Glaciers*. Cambridge, U.K.: Cambridge Univ. Press, 2002.

[3] G. Kaser and C. Georges, "Changes of the equilibrium-line altitude in the tropical Cordillera Blanca, Peru, 1930–50, and their spatial variations," *Ann. Glaciol.*, vol. 24, pp. 344–349, 1997, doi: 10.3189/S0260305500012428.

[4] I. Dussaillant et al., "Two decades of glacier mass loss along the Andes," *Nat. Geosci.*, vol. 12, no. 10, pp. 802–808, Oct. 2019, doi: 10.1038/s41561-019-0432-5.

[5] B. G. Mark and G. O. Seltzer, "Tropical glacier meltwater contribution to stream discharge: A case study in the Cordillera Blanca, Peru," *J. Glaciol.*, vol. 49, no. 165, pp. 271–281, 2003, doi: 10.3189/172756503781830746.

[6] R. Bindschadler, "The importance of pressurized subglacial water in separation and sliding at the glacier bed," *J. Glaciol.*, vol. 29, no. 101, pp. 3–19, 1983, doi: 10.3189/S0022143000005104.

[7] B. de Fleurian et al., "A modeling study of the effect of runoff variability on the effective pressure beneath Russell Glacier, West Greenland," *JGR Earth Surf.*, vol. 121, no. 10, pp. 1834–1848, Oct. 2016, doi: 10.1002/2016JF003842.

[8] J. T. Harper, N. F. Humphrey, W. T. Pfeffer, and B. Lazar, "Two modes of accelerated glacier sliding related to water," *Geophysical Res. Lett.*, vol. 34, no. 12, Jun. 2007, Art. no. L12503, doi: 10.1029/2007GL030233.

[9] A. Iken and R. A. Bindschadler, "Combined measurements of subglacial water pressure and surface velocity of Findelengletscher, Switzerland: Conclusions about drainage system and sliding mechanism," *J. Glaciol.*, vol. 32, no. 110, pp. 101–119, 1986, doi: 10.3189/S0022143000006936.

[10] A. Kääb et al., "Sudden large-volume detachments of low-angle mountain glaciers—More frequent than thought?," *Cryosphere*, vol. 15, no. 4, pp. 1751–1785, Apr. 2021, doi: 10.5194/tc-15-1751-2021.

[11] J. Faillettaz, M. Funk, and C. Vincent, "Avalanching glacier instabilities: Review on processes and early warning perspectives," *Rev. Geophys.*, vol. 53, no. 2, pp. 203–224, Jun. 2015, doi: 10.1002/2014RG000466.

[12] C. Vincent and L. Moreau, "Sliding velocity fluctuations and subglacial hydrology over the last two decades on Argentière glacier, Mont Blanc area," *J. Glaciol.*, vol. 62, no. 235, pp. 805–815, Oct. 2016, doi: 10.1017/jog.2016.35.

[13] C. Schoof, "Ice-sheet acceleration driven by melt supply variability," *Nature*, vol. 468, no. 7325, pp. 803–806, Dec. 2010, doi: 10.1038/nature09618.

[14] T. C. Bartholomaus, R. S. Anderson, and S. P. Anderson, "Response of glacier basal motion to transient water storage," *Nature Geosci*, vol. 1, no. 1, pp. 33–37, Jan. 2008, doi: 10.1038/ngeo.2007.52.

[15] A. Iken, "The effect of the subglacial water pressure on the sliding velocity of a glacier in an idealized numerical model," *J. Glaciol.*, vol. 27, no. 97, pp. 407–421, 1981, doi: 10.3189/S0022143000011448.

[16] M. Hoffman and S. Price, "Feedbacks between coupled subglacial hydrology and glacier dynamics," *J. Geophys. Res. Earth Surf.*, vol. 119, no. 3, pp. 414–436, Mar. 2014, doi: 10.1002/2013JF002943.

[17] V. C. Tsai, L. C. Smith, A. S. Gardner, and H. Seroussi, "A unified model for transient subglacial water pressure and basal sliding," *J. Glaciol.*, vol. 68, no. 268, pp. 390–400, Apr. 2022, doi: 10.1017/jog.2021.103.

[18] B. Francou, M. Vuille, V. Favier, and B. Cáceres, "New evidence for an ENSO impact on low-latitude glaciers: Antizana 15, Andes of Ecuador, 0°28′S," *J. Geophys. Res.*, vol. 109, no. D18, Sep. 2004, Art. no. D18106, doi: 10.1029/2003JD004484.

[19] F. Maussion, W. Gurgiser, M. Großhauser, G. Kaser, and B. Marzeion, "ENSO influence on surface energy and mass balance at Shallap Glacier, Cordillera Blanca, Peru," *Cryosphere*, vol. 9, no. 4, pp. 1663–1683, Aug. 2015, doi: 10.5194/tc-9-1663-2015.

[20] W. Blake, U. H. Fischer, C. R. Bentley, and G. K. G. Clarke, "Instruments and methods: Direct measurement of sliding at the glacier bed," *J. Glaciol.*, vol. 40, no. 136, pp. 595–599, 1994, doi: 10.3189/S002214300001248X.

[21] J. Weertman, "The Theory of Glacier Sliding," *J. Glaciol.*, vol. 5, no. 39, pp. 287–303, 1964, doi: 10.3189/S0022143000029038.

[22] Mountain Research Initiative EDW Working Group,"Elevation-dependent warming in mountain regions of the world," *Nature Clim. Change*, vol. 5, no. 5, pp. 424–430, May 2015, doi: 10.1038/nclimate2563.

[23] M. Carey, "Living and dying with glaciers: People's historical vulnerability to avalanches and outburst floods in Peru," *Glob. Planet. Change*, vol. 47, no. 2–4, pp. 122–134, Jul. 2005, doi: 10.1016/j.gloplacha.2004.10.007.

[24] J. L. Carrivick and F. S. Tweed, "A global assessment of the societal impacts of glacier outburst floods," *Glob. Planet. Change*, vol. 144, pp. 1–16, 2016, doi: 10.1016/j.gloplacha.2016.07.001.

[25] C. Huggel, W. Haeberli, A. Kääb, D. Bieri, and S. Richardson, "An assessment procedure for glacial hazards in the Swiss Alps," *Can. Geotechnical J.*, vol. 41, pp. 1068–1083, 2004, doi: 10.1139/t04-053.

[26] A. Schubert, A. Faes, A. Kääb, and E. Meier, "Glacier surface velocity estimation using repeat TerraSAR-X images: Wavelet- vs. correlation-based image matching," *ISPRS J. Photogrammetry Remote Sens.*, vol. 82, pp. 49–62, Aug. 2013, doi: 10.1016/j.isprsjprs.2013.04.010.

[27] T. Strozzi, A. Luckman, T. Murray, U. Wegmuller, and C. L. Werner, "Glacier motion estimation using SAR offset-tracking procedures," *IEEE Trans. Geosci. Remote Sens.*, vol. 40, no. 11, pp. 2384–2391, Nov. 2002, doi: 10.1109/TGRS.2002.805079.

[28] S. H. Winsvold, A. Kääb, C. Nuth, L. M. Andreassen, W. J. J. van Pelt, and T. Schellenberger, "Using SAR satellite data time series for regional glacier mapping," *Cryosphere*, vol. 12, no. 3, pp. 867–890, Mar. 2018, doi: 10.5194/tc-12-867-2018.

[29] *Japan Aerospace Exploration Agency and Earth Observation Research Center (EORC)*, ALOS—Advanced Land Observing Satellite; ALOS Research and Applictaion Project. JAXA, 2023. Accessed: Feb. 23, 2024. [Online]. Available: https://www.eorc.jaxa.jp/ALOS/en/dataset/aw3d30/aw3d30_e.htm

[30] A. Kos et al., "The surface velocity response of a tropical glacier to intra and inter annual forcing, Cordillera Blanca, Peru," *Remote Sens.*, vol. 13, no. 14, Jul. 2021, Art. no. 2694, doi: 10.3390/rs13142694.

[31] "Copernicus Global Digital Elevation Model (GLO-30)," European Space Agency, 2024, doi: 10.5069/G9028PQB.

[32] "Randolph Glacier Inventory—A dataset of Global Glacier Outlines, version 6.0," RGI Consortium, 2017, doi: 10.7265/4m1f-gd79.

[33] "Randolph Glacier Inventory—A dataset of Global Glacier Outlines, version 7.0," RGI Consortium, 2023, doi: 10.5067/F6JMOVY5NAVZ.

[34] J. J. Mohr, N. Reeh, and S. N. Madsen, "Three-dimensional glacial flow and surface elevation measured with radar interferometry," *Nature*, vol. 391, no. 6664, pp. 273–276, Jan. 1998, doi: 10.1038/34635.

[35] GAMMA Remote Sensing Research and Consulting AG, "GAMMA Remote Sensing," Accessed: Aug. 03, 2024. [Online]. Available: https://www.gamma-rs.ch/

[36] R. Michel and E. Rignot, "Flow of Glaciar Moreno, Argentina, from repeat-pass Shuttle Imaging Radar images: Comparison of the phase correlation method with radar interferometry," *J. Glaciol.*, vol. 45, no. 149, pp. 93–100, 1999, doi: 10.3189/S0022143000003075.

[37] F. Paul et al., "The glaciers climate change initiative: Methods for creating glacier area, elevation change and velocity products," *Remote Sens. Environ.*, vol. 162, pp. 408–426, Jun. 2015, doi: 10.1016/j.rse.2013.07.043.

[38] T. Schellenberger, T. Dunse, A. Kääb, J. Kohler, and C. H. Reijmer, "Surface speed and frontal ablation of Kronebreen and Kongsbreen, NW Svalbard, from SAR offset tracking," *Cryosphere*, vol. 9, no. 6, pp. 2339–2355, Dec. 2015, doi: 10.5194/tc-9-2339-2015.

[39] F. T. Ulaby, R. K. Moore, and A. K. Fung, *Microwave Remote Sensing: Active and Passive. Volume 2: Radar remote Sensing and Surface Scattering and Emission Theory*, vol. 2. Reading, MA, USA: Addison-Wesley, 1982.

[40] S. Abdullahi, B. Wessel, M. Huber, A. Wendleder, A. Roth, and C. Kuenzer, "Estimating penetration-related X-band InSAR elevation bias: A study over the Greenland ice sheet," *Remote Sens.*, vol. 11, no. 24, Dec. 2019, Art. no. 2903, doi: 10.3390/rs11242903.

[41] H. Rott and C. Mätzler, "Possibilities and limits of synthetic aperture radar for snow and glacier surveying," *A. Glaciol.*, vol. 9, pp. 195–199, 1987, doi: 10.3189/S0260305500000604.

[42] S. Leinss and P. Bernhard, "TanDEM-X:Deriving InSAR height changes and velocity dynamics of Great Aletsch Glacier," *IEEE J. Sel. Top. Appl. Earth Observ. Remote Sens.*, vol. 14, pp. 4798–4815, 2021, doi: 10.1109/JSTARS.2021.3078084.

[43] T. Nagler and H. Rott, "Retrieval of wet snow by means of multitemporal SAR data," *IEEE Trans. Geosci. Remote Sens.*, vol. 38, no. 2, pp. 754–765, Mar. 2000, doi: 10.1109/36.842004.

[44] F. T. Ulaby, R. K. Moore, and A. K. Fung, *Microwave Remote Sensing: Active and Passive. Volume 3: From theory to Applications*, vol. 3. Dedham, MA, USA: Artech House, 1986.

[45] F. Crameri, "Scientific colour maps," Zenodo, Oct. 2023, doi: 10.5281/zenodo.8409685.

[46] R. Millan et al., "Mapping surface flow velocity of glaciers at regional scale using a multiple sensors approach," *Remote Sens.*, vol. 11, no. 21, Oct. 2019, Art. no. 2498, doi: 10.3390/rs11212498.

[47] D. I. Benn and D. J. A. Evans, *Glaciers & Glaciation*, 2nd ed. London, U.K.: Hodder education, 2010.

[48] K. A. Lamantia, L. J. Larocca, L. G. Thompson, and B. G. Mark, "El Niño enhances snow-line rise and ice loss on the Quelccaya Ice Cap, Peru," *Cryosphere*, vol. 18, no. 10, pp. 4633–4644, Oct. 2024, doi: 10.5194/tc-18-4633-2024.

[49] L. Mourre et al., "Spatio-temporal assessment of WRF, TRMM and in situ precipitation data in a tropical mountain environment (Cordillera Blanca, Peru)," *Hydrol. Earth Syst. Sci.*, vol. 20, no. 1, pp. 125–141, Jan. 2016, doi: 10.5194/hess-20-125-2016.

[50] J. Lund, R. R. Forster, E. J. Deeb, G. E. Liston, S. M. Skiles, and H.-P. Marshall, "Interpreting sentinel-1 SAR backscatter signals of snowpack surface melt/freeze, warming, and ripening, through field measurements and physically-based SnowModel," *Remote Sens.*, vol. 14, no. 16, Aug. 2022, Art. no. 4002, doi: 10.3390/rs14164002.

[51] C. Marin et al., "Use of Sentinel-1 radar observations to evaluate snowmelt dynamics in alpine regions," *Cryosphere*, vol. 14, no. 3, pp. 935–956, Mar. 2020, doi: 10.5194/tc-14-935-2020.

[52] T. Strozzi, A. Wiesmann, and C. Mätzler, "Active microwave signatures of snow covers at 5.3 and 35 GHz," *Radio Sci.*, vol. 32, no. 2, pp. 479–495, Mar. 1997, doi: 10.1029/96RS03777.

[53] C. Scher, N. C. Steiner, and K. C. McDonald, "Mapping seasonal glacier melt across the Hindu Kush Himalaya with time series synthetic aperture radar (SAR)," *Cryosphere*, vol. 15, no. 9, pp. 4465–4482, Sep. 2021, doi: 10.5194/tc-15-4465-2021.

[54] G. E. Flowers, "Glacier hydromechanics: Early insights and the lasting legacy of three works by Iken and colleagues," *J. Glaciol.*, vol. 56, no. 200, pp. 1069–1078, 2010, doi: 10.3189/002214311796406103.

[55] A. G. Fountain and J. S. Walder, "Water flow through temperate glaciers," *Rev. Geophys.*, vol. 36, no. 3, pp. 299–328, Aug. 1998, doi: 10.1029/97RG03579.

[56] B. Kamb, "Sliding motion of glaciers: Theory and observation," *Rev. Geophys.*, vol. 8, no. 4, pp. 673–728, Nov. 1970, doi: 10.1029/RG008i004p00673.

[57] G. Kaser, I. Juen, C. Georges, J. Gómez, and W. Tamayo, "The impact of glaciers on the runoff and the reconstruction of mass balance history from hydrological data in the tropical Cordillera Blanca, Perú," *J. Hydrol.*, vol. 282, no. 1–4, pp. 130–144, Nov. 2003, doi: 10.1016/S0022-1694(03)00259-2.
[58] W. Gurgiser, B. Marzeion, L. Nicholson, M. Ortner, and G. Kaser, "Modeling energy and mass balance of Shallap Glacier, Peru," *Cryosphere*, vol. 7, no. 6, pp. 1787–1802, Nov. 2013, doi: 10.5194/tc-7-1787-2013.
[59] C. Aubry-Wake, D. Zéphir, M. Baraer, J. M. McKENZIE, and B. G. Mark, "Importance of longwave emissions from adjacent terrain on patterns of tropical glacier melt and recession," *J. Glaciol.*, vol. 64, no. 243, pp. 49–60, Feb. 2018, doi: 10.1017/jog.2017.85.
[60] M. H. Braun et al., "Constraining glacier elevation and mass changes in South America," *Nature Clim. Change*, vol. 9, no. 2, pp. 130–136, Feb. 2019, doi: 10.1038/s41558-018-0375-7.
[61] T. Seehaus, P. Malz, C. Sommer, S. Lippl, A. Cochachin, and M. Braun, "Changes of the tropical glaciers throughout Peru between 2000 and 2016—Mass balance and area fluctuations," *Cryosphere*, vol. 13, no. 10, pp. 2537–2556, Sep. 2019, doi: 10.5194/tc-13-2537-2019.
[62] R. Fallourd et al., "Monitoring temperate glacier displacement by multi-temporal TerraSAR-X images and continuous GPS measurements," *IEEE J. Sel. Top. Appl. Earth Observ. Remote Sens.*, vol. 4, no. 2, pp. 372–386, Jun. 2011, doi: 10.1109/JSTARS.2010.2096200.
[63] R. Kenner et al., "Factors controlling velocity variations at short-term, seasonal and multiyear time scales, Ritigraben Rock Glacier, Western Swiss Alps," *Permafrost Periglacial*, vol. 28, no. 4, pp. 675–684, Oct. 2017, doi: 10.1002/ppp.1953.
[64] C. L. Fyffe et al., "The energy and mass balance of Peruvian glaciers," *JGR Atmos.*, vol. 126, no. 23, Dec. 2021, Art. no. e2021JD034911, doi: 10.1029/2021JD034911.
[65] R. Basantes-Serrano et al., "New insights into the decadal variability in glacier volume of a tropical ice cap, Antisana (0°29′ S, 78°09′ W), explained by the morpho-topographic and climatic context," *Cryosphere*, vol. 16, no. 11, pp. 4659–4677, Nov. 2022, doi: 10.5194/tc-16-4659-2022.
[66] U. Nanni, D. Scherler, F. Ayoub, R. Millan, F. Herman, and J.-P. Avouac, "Climatic control on seasonal variations in mountain glacier surface velocity," *Cryosphere*, vol. 17, no. 4, pp. 1567–1583, Apr. 2023, doi: 10.5194/tc-17-1567-2023.
[67] R. Culberg, R. J. Michaelides, and J. Z. Miller, "Sentinel-1 detection of ice slabs on the Greenland Ice Sheet," *Cryosphere*, vol. 18, no. 5, pp. 2531–2555, May 2024, doi: 10.5194/tc-18-2531-2024.
[68] T. Seehaus, A. J. Cook, A. B. Silva, and M. Braun, "Changes in glacier dynamics in the northern Antarctic Peninsula since 1985," *Cryosphere*, vol. 12, no. 2, pp. 577–594, Feb. 2018, doi: 10.5194/tc-12-577-2018.



Hannes Beier received the M.Sc. degree in applied geosciences from the RWTH Aachen University, Aachen, Germany, in 2021.

Since 2021, he has been a Research Assistant/Ph.D. Student with the Chair of Engineering Geology and Hydrogeology, RWTH Aachen University, Aachen, Germany. From 2019 to 2023, he was a Technical Assistant with the Ingenieurbüro O. Goldbach, Germany. His research interests include radar remote sensing, cryosphere and glacier dynamics, slope instability and permafrost processes, and rock mechanics.



Tazio Strozzi (Senior Member, IEEE) received the M.S. and Ph.D. degrees in physics from the University of Bern, Bern, Switzerland, in 1993 and 1996, respectively, for his experimental and theoretical studies on the backscattering characteristics of snow and vegetation.

He has been with the Gamma Remote Sensing AG, Switzerland, since 1996, where he is responsible for the development of radar remote sensing applications and is the Manager of a number of research and commercial projects. From 1996 to 1998, he was a part-time physics Teacher with the Highschool of Bellinzona, Bellinzona, Switzerland. From 1999 to 2001, he worked as a part-time Visiting Scientist with the University of Wales, Swansea, U.K. His research interests include SAR and SAR interferometry for land use applications (including permafrost, forest, snow cover, and hazard mapping) and differential SAR interferometry for subsidence monitoring, glacier motion estimation, and landslide surveying.



Julian Osten received the M.Sc. degree in applied geosciences from the RWTH Aachen University, Aachen, Germany, in 2022. He is currently working toward the Ph.D. degree in geomechanics with the Department of Engineering Geology and Hydrogeology, RWTH Aachen University, Aachen, Germany.

His research interests include remote sensing, rock mechanics, and induced seismicity.



Andrew Kos (Member, IEEE) received the B.Sc. and Ph.D. degrees in geology from the Monash University, Melbourne, VIC, Australia, in 1994 and 1999, respectively.

He is currently an Earth Scientist applying Earth observation and geospatial analytics to environmental monitoring, climate-risk assessment, and natural-hazard management. He is the Founder and Managing Director of the Terrasense Switzerland AG, an ETH Zurich spin-off, where he leads applied research and international consulting projects at the interface of remote sensing, engineering geology, and decision support. He has worked internationally with government agencies, multilateral organizations, and research partners on environmental monitoring, multihazard risk assessment, and early-warning readiness in mountain and climate-sensitive regions. His research interests include the integration of satellite EO, in-situ sensors, terrestrial remote sensing, and process-based interpretation for geophysical process monitoring, hazard assessment, and operationally risk and resilience applications.



Florian Amann received the Dipl.-Geol. (M.Sc.) degree in geology from the Friedrich-Alexander-Universität Erlangen-Nürnberg, Erlangen, Germany, in 2002, and the Ph.D. degree in engineering geology from the Friedrich-Alexander-Universität Erlangen-Nürnberg, Erlangen, Germany, in 2006.

His major field of study was engineering geology with a focus on rock mechanics and hydrogeology. He worked with the Pöyry Infra/Pöyry Energy AG, Switzerland, from 2002 to 2007. From 2007 to 2016, he was a Senior Research Associate (Oberassistent) in Engineering Geology with the ETH Zürich, Zürich, Switzerland. Between 2011 and 2014, he was a Scientist with the Rio Tinto Center for Underground Mine Construction, Sudbury, ON, Canada. From 2015 to 2017, he served as a Scientific Director with the Deep Underground Geothermal Laboratory, ETH Zürich. Since 2017, he has been a Chair Professor of Engineering Geology with the RWTH Aachen University, Aachen, Germany. His research interests include unstable rock slopes and natural hazards, rock and geomechanics, nuclear waste repositories, deep geothermal energy, thermohydromechanically coupled processes in rock, periglacial rock slope dynamics, permafrost in rock, and hydraulic stimulations. He is active in the field of engineering geology and geomechanics and contributes to interdisciplinary research initiatives related to subsurface energy systems and geohazards.